Journal of Alloys and Compounds 509 (2011) 1463–1470

Contents lists available at ScienceDirect

Journal of Alloys and Compounds

journal homepage: www.elsevier.com/locate/jallcom

Aerosol synthesis and Rietveld analysis of tetragonal (β_1) PdZn

Eric J. Peterson[a], Barr Halevi[a], Boris Kiefer[a,b], Michael N. Spilde[a], Abhaya K. Datye[a,*], Joe Peterson[b], Luc Daemen[c], Anna Llobet[c], Heinz Nakotte[b,c]

[a] Department of Chemical and Nuclear Engineering and Center for Microengineered Materials, MSC01 1120, University of New Mexico, Albuquerque, NM 87131-0001, USA
[b] Department of Physics, New Mexico State University, Las Cruces, NM 88003, USA
[c] Los Alamos National Laboratory, Manuel Lujan Neutron Science Center, P.O. Box 1663, Los Alamos, NM 87545, USA

ARTICLE INFO

Article history:
Received 13 May 2010
Received in revised form 17 August 2010
Accepted 6 September 2010
Available online 8 December 2010

Keywords:
PdZn
Catalysis
Crystal structure
Order–disorder effects
Phase diagrams
Neutron
Diffraction
Thermal analysis
X-ray diffraction
Scanning electron microscopy
SEM
Intermetallics
Transition metal alloys and compounds

ABSTRACT

The β_1 PdZn intermetallic of nominal 50:50 Pd:Zn at% was synthesized using an aerosol method. The aerosol method provided atomically mixed precursor oxy-nitrate powder that was then reduced to form β_1 PdZn, having a surface area amenable to catalytic measurements. Formation of the β_1 PdZn during reduction was found to occur rapidly (4 h) and at moderate temperature (500 °C), serving to minimize the loss of volatile Zn. Chemical and structural characterization confirms that β_1 PdZn (95–99 wt% phase pure) of the same composition as the nitrate feedstock solution can be prepared using this method. Detailed structural analysis shows that this material contains little or no vacancies and minimal Pd/Zn disorder.

1. Introduction

The tetragonal PdZn intermetallic compound of approximate composition 50% (atomic) Zn is currently of interest as a methanol steam reforming (MSR) catalyst for proton exchange membrane (PEM) fuel cells [1]. The catalyst used for this reaction is Pd supported on ZnO, but the PdZn phase forms *in-situ* during reduction in H_2 and also during reaction, since H_2 is a product of methanol steam reforming [2]. The conversion of Pd to PdZn causes the MSR reaction to switch from 100% selectivity toward CO (on Pd) to nearly 100% selectivity towards CO_2 [3]. This is of crucial importance in the case of PEM fuel cells, as CO is a known poison in this application. The catalyst that is currently in use commercially for this application is ZnO-supported Cu. It has been noted that PdZn exhibits a similar valence electron density of states (DOS) to that of Cu metal, and suggested that this is the reason for the observed similarity in catalytic behavior between the two phases [4,5]. However, Cu metal suffers from deactivation with time, a result of surface area loss due to sintering of the metal particles. The PdZn catalyst can be regenerated easily, making it a viable alternative [2].

The PdZn phase is therefore of interest for the MSR reaction; however, XRD and TEM show that the working catalyst contains Pd, PdZn and ZnO phases [6]. It is difficult to identify the role of each of these phases in supported catalysts. Furthermore, the relatively low abundance of the PdZn compared to that of the ZnO support makes it difficult to acquire high quality structural data. It was therefore decided to synthesize bulk, unsupported PdZn for structural characterization by X-ray and neutron powder diffraction methods. A requirement was that the bulk PdZn posses sufficient surface area for reasonable catalytic measurements, precluding traditional monolithic metallurgical synthesis techniques. Volatility of Zn under reducing conditions is an additional challenge during synthesis of PdZn phases of controlled composition. With these factors in mind, an aerosol synthesis route [7] was chosen for the production of bulk PdZn powder. The resulting material was then

* Corresponding author at: University of New Mexico, Department of Chemical and Nuclear Engineering and Center for Microengineered Materials, Chemical and Nuclear Engineering, MSCO1 1120, Albuquerque, NM 87131, USA.
Tel.: +1 505 277 2833; fax: +1 505 277 1024.
E-mail address: datye@unm.edu (A.K. Datye).

0925-8388/$ – see front matter © 2010 Elsevier B.V. All rights reserved.
doi:10.1016/j.jallcom.2010.09.149

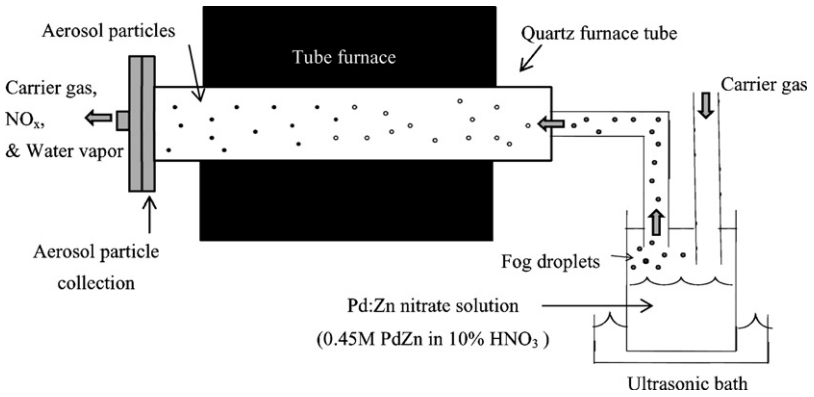

Fig. 1. A schematic diagram of the aerosol powder synthesis apparatus. The ultrasonic vibrations from the ultrasonic bath are transmitted to the Pd–Zn nitrate solution via a plastic diaphragm, causing the formation of fog droplets.

examined by Rietveld analysis coupled with electron microprobe analysis. Because defects are known to play an important role in many catalytic systems, attention was focused on evaluation of the type and quantity of defects in β_1 PdZn. These experiments were augmented with density-functional-theory calculations to independently investigate the energetics of Pd ↔ Zn disorder in β_1 PdZn.

An additional motivation for this work was the lack of an accurate experimental reference X-ray diffraction pattern for β_1 PdZn. The current X-ray diffraction reference patterns for β_1 PdZn are an experimental pattern (PDF number 00-006-0620) and a calculated pattern (PDF number 01-072-2936). Both patterns are based on the same reference [8], yet disagree with one another as to relative peak intensities. In this paper we present experimental data that is in good agreement with the calculated pattern.

2. Experimental

The PdZn precursor powder was synthesized using an aerosol method employing a metal nitrate feed solution. A 1:1 Pd:Zn nitric acid solution was prepared by mixing equimolar volumes of Pd and Zn dissolved in nitric acid. The Pd–nitrate solution was obtained from Aldrich, and was composed of 4.5 wt% Pd in 10 vol.% nitric acid. An equimolar solution of Zn was prepared by weighing and dissolving $Zn(NO_3)_2{\cdot}6H_2O$ (Aldrich) in 10 vol.% nitric acid. Equal volumes of Pd and Zn solutions were measured into a flask using an Ependorff pipette to produce 1:1 PdZn in 10 vol.% nitric acid. A schematic diagram of the aerosol system is shown in Fig. 1. The aerosol vapor was produced by immersing a cylindrical glass tube, with a plastic diaphragm on the bottom, into the water reservoir of a Walgreen-brand ultrasonic humidifier. The ultrasonic waves propagating through the plastic diaphragm produced a fog of metal nitrate droplets, which were swept from the glass tube by a nitrogen carrier gas flowing at 1 l/min through an 80 cm-long 3-zone tube furnace with a 2.54 cm O.D. quartz furnace tube. The furnace zone temperatures were set at 800 °C at the furnace entrance zone, 800 °C in the middle, and 550 °C at the exit zone. During the transit through the furnace, the solvent in the fog droplets was lost, converting droplets into roughly spherical solid particles. The reactor system was allowed to run until approximately 90% of the nitrate solution was expended. The damp powder was collected at the furnace exit on a filter, where it was allowed to dry, under flowing N_2, after the aerosol generator was turned off. The resulting cake was scraped from the filter paper and then subjected to a reduction treatment (4 h at 500 °C in flowing 5% H_2/balance N_2).

The powder surface area was determined by nitrogen adsorption at 77 K using a Micromeritics Gemini System and Quantachrome Autosorb 1-C/TCD. The samples were outgassed at 120 °C for 5+ h under vacuum before measurements. The surface areas were determined from adsorption values using a five point BET analysis at P/P_0 ranging from 0.05 to 0.2. Thermogravimetric analysis (TA model STQ600) was performed on the as-produced aerosol powder under atmospheres of air, N_2, and H_2/N_2. Scanning electron microscopy (SEM) images of the PdZn powder were acquired using a Hitachi S-5200 SEM. The powder was ground lightly in an alumina mortar and pestle to break up clumps, and then pressed onto carbon double-stick tape that had been adhered to an aluminum sample holder. Secondary and backscatter electron images of the polished mount were also collected using an FEI FIB operating at 30 keV. Electron probe microanalysis (EPMA) was performed on a pressed pellet of the PdZn powder that had been mounted in epoxy and polished, with increasingly finer grits, down to 0.3 μm-grit Al_2O_3 polishing compound. The sample was coated with a 15–20 nm thick layer of evaporated carbon, which was nominally the same thickness of carbon coating on the standards that were used in the analysis. Data was collected using a JEOL 8200 microprobe operating at 20 kV and 20 nA with a takeoff angle of 40°. Quantitative analysis was performed using wavelength dispersive spectrometry, employing pentaerythritol (PETL), lithium fluoride (LIFH), and layered dispersive element (LDE1) crystal monochromators for the measurement of the Pd L-α, Zn K-α, and O-Kα peaks, respectively. Standard intensities were measured from elemental Pd and $ZnAl_2O_4$ standards, and the pulse-height analyzer for the spectrometer measuring the O-Kα peak (0.525 keV) was optimized to minimize interference from the Pd Mγ peak (0.522 keV). A ZAF correction was applied to the data to account for the effects of atomic number, absorption, and secondary fluorescence. To obtain a representative chemical characterization of the sample, analyses were collected on a grid, with 50 μm spacing between grid points.

Neutron powder (NPD) diffraction was performed on the HIPD instrument at the Los Alamos Neutron Science Center. Time-of-flight neutron data was collected at 4 K from detector banks at ±14°, ±40°, ±90° and ±153°. X-ray diffraction data was then collected at room temperature on the same sample using a Rigaku Ultima III θ–θ diffractometer equipped with a Cu-target X-ray tube (Cu $K\alpha_1$ = 1.540562 Å, Cu $K\alpha_2$ = 1.544390 Å) [9] and a graphite monochromator for the removal of Cu K-β radiation. The sample was loaded into a zero-background sample holder, and data was collected over a scan range of 5–148° 2θ with a step size of 0.02° and a scan rate of 0.1 °/min. To obtain an accurate room temperature lattice parameter, a portion of the sample was then mixed with silicon standard SRM640b and a second X-ray diffraction data set was collected using a Scintag PADV θ–2θ diffractometer, also equipped with a Cu-target X-ray tube and a graphite monochromator. The sample was distributed in a thin layer on a lightly-greased quartz zero background plate, and data was collected over a range of 20–95° 2θ with a step size of 0.02° and a count time of 12 s per step. Rietveld analysis of the neutron and X-ray powder diffraction data was performed using the software package GSAS [10], employing an anisotropic microstrain model in the peak profile function [11]. In the case of the neutron Rietveld refinements, only data from the four high angle detector banks was used (±90° and ±153°), due to their relatively high resolution (0.5% and 0.3%, respectively) compared to that of the four low angle detector banks (±14 (3%) and ±40 (1.0%)°). X-ray and neutron scattering factors [12] are listed in Table 1. It is apparent that while for X-ray scattering there is good contrast between Pd and Zn, in the case of neutron scattering there is only slight contrast between these two elements.

We augmented our experiments with first-principle calculations that are based on density-functional-theory [13] as implemented in the periodic structure software package VASP [14–16]. Electronic exchange and correlations were treated at the GGA level within the parameterization of Perdew et al. [17]. The interactions between electrons and nuclei were described within the PAW formalism [18,19]. The electronic configurations (core radii in atomic units, $1a_B$ = 0.529 Å, in parentheses) were $5s^2 4p^6 3d^8$ (2.300 a_B), $3d^{10} 4s^2$ (2.400 a_B), for Pd, and Zn, respectively. The FERMI-level was slightly broadened using 1st order Methfessel and Paxton broadening (σ = 0.1 eV)[20], a typical value for metallic systems. All calculations were

Table 1
X-ray (XRD) atomic number and neutron (NPD) scattering lengths and cross-sections.

	Z	Bound coherent scattering length (fm)	Bound coherent scattering cross section (barn)	Total bound scattering cross section (barn)
Pd	46	5.91	4.39	4.48
Zn	30	5.680	4.054	4.131
Ratio	1.5	1.04	1.08	1.08

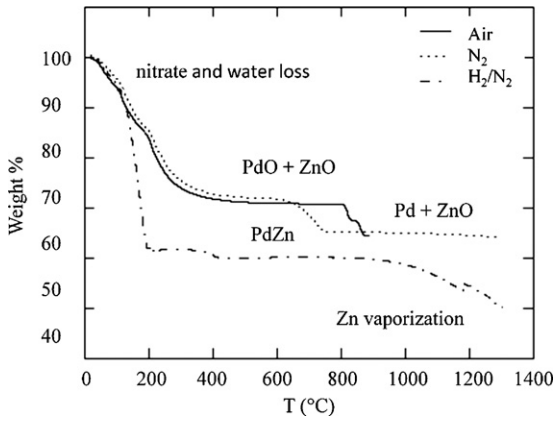

Fig. 2. Thermogravimetric analyzer (TGA) data obtained from as-produced PdZn aerosol powder.

performed using a cutoff energy of E_{cut} = 600 eV which was found to be sufficient to obtain converged results. The density of the k-point mesh [21] was adjusted such that results were converged to within 1 meV/atom. For $Pd_{50}Zn_{50}$ in the conventional four atom cell we employed a 16 × 16 × 16 *k*-point grid. In order to investigate site-disorder in $Pd_{50}Zn_{50}$ we employed 2 × 2 × 2 supercells of the tP4 representation of this phase, containing a total of 32 atoms, and a 8 × 8 × 8 *k*-point grid. During geometry optimization all degrees of freedom, lattice parameters and internal coordinates were relaxed simultaneously. The component PAW potentials were tested for elemental Pd and Zn metals. The optimized equilibrium lattice parameter for fcc-Pd is a = 3.958 Å (16 × 16 × 16 *k*-point grid), consistent with previous work [5], and for elemental hcp-Zn (19 × 19 × 11 *k*-point grid), we obtain a = 2.665 Å, and c = 4.954 Å. For comparison the experimental lattice parameters are, a = 3.891 Å, and a = 2.665 Å and c = 4.947 Å, for fcc-Pd and hcp-Zn, respectively [22]. This 1–2% overestimation of the lattice parameters is typical for calculations at the GGA-level [19].

3. Results and discussion

3.1. Powder characterization

Fig. 2 shows the results of TGA analysis of as-produced aerosol powder under air, N_2, and H_2/N_2. Onset of reduction of PdO to Pd metal was observed at 650 °C under N_2, and at 800 °C under air. In the H_2/N_2 mixture, complete reduction of ZnO and PdO was observed to have occurred by 400 °C with weight loss, resulting from Zn volatility, becoming apparent after approximately 900 °C. Based on these TGA results, the as-produced aerosol powder was reduced in flowing H_2/N_2 in a furnace at 500 °C for 4 h to produce the PdZn phase. Fig. 3 shows secondary electron images of the aerosol powder after reduction. The BET surface area of the powder was 4.7 m^2/g, corresponding to a 126 nm mean particle diameter [23], which is consistent with the SEM image. Electron backscatter and secondary electron images of the polished sample are shown in Fig. 4. The electron backscatter image is sensitive to average atomic number differences, with Pd-rich regions appearing as lighter-shade areas in the backscatter image. Electron microprobe analyses were performed at grid points as shown in Fig. 4A. Electron microprobe results are summarized in Table 2, and Fig. 5 is a histogram showing the distribution of Zn compositions, with a mean of 49.6 at% Zn, which is quite close to the nominal, as-prepared composition of 50 at% Zn. The Pd-rich regions were found to be approximately 1 at% richer in Pd than average. The standard deviation of 100 electron microprobe analyses was found to be 0.3% (atomic), yielding a 95% confidence limit of ±0.06%, demonstrating that the aerosol method is capable of creating powders of a fairly uniform chemical composition that is essentially identical to that of the feedstock nitrate solution. The approximately 3% oxygen (weight) in the analysis is likely due to the presence of a surface oxide. Because the crystallite sizes were significantly smaller than the approximately 1 μm^3 electron probe excitation volume, these results represent the average bulk chemical composition of the sample.

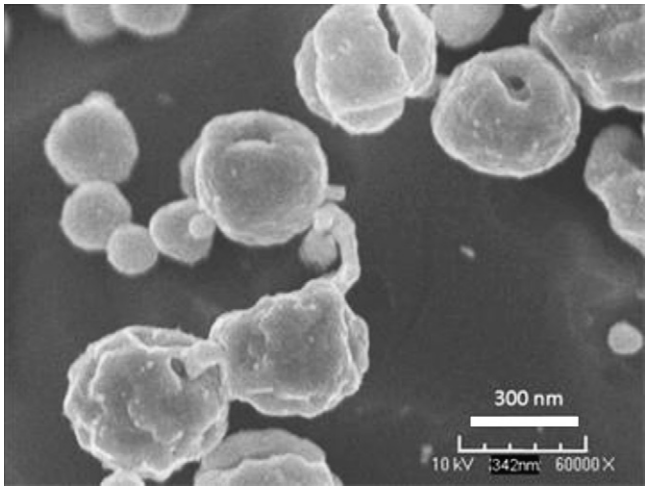

Fig. 3. Scanning electron micrograph (secondary electron image) of the PdZn aerosol powder, reduced at 500 °C for 4 h in flowing 5% H_2/N_2.

Table 2
Electron microprobe analysis results. Average of 100 analyses (1σ standard deviation).

	Pd	Zn	O	Total
Weight%	60.8(5)	36.7(4)	3.2(4)	100.7(5)
Atom%	50.4(3)	49.6(3)		100

3.2. Structural characterization

Fig. 6A shows the X-ray diffraction data (degrees 2θ), and Fig. 6B is a comparison of the X-ray diffraction data to the neutron diffraction data (*d*-space (Å)), with the observed and the calculated and difference plots from the final Rietveld refinements. Although it was possible to fit all of the X-ray diffraction peaks using the tetragonal β_1 PdZn structure, small but distinct peaks in the neutron diffraction pattern at 2.14 and 1.51 Å were found to be consistent with the presence of a cubic phase, having a lattice parameter of 3.0234(5) Å.

3.2.1. Cubic phase

The PdZn phase diagram [24–27] shows that the tetragonal β_1 PdZn phase of interest is bracketed by the cubic β'' (Pd-rich) and β' (Zn-rich) [28] phases at temperatures greater than 600–650 °C, and by lower symmetry δ (Pd-rich) [29] and ε (Zn-rich) [30] phases at room temperature [26]. The two unindexed peaks in the neutron diffraction data could not be indexed by either of the room temperature phases, but were consistent in both position and intensity with one of the two cubic phases. The two cubic phases have been described as being Strukturbericht type B2 (CsCl), and to a first approximation can be thought of as the inverse of one another. Interestingly, the lattice parameters of these two phases are quite similar (3.04–3.06 Å for the Pd-rich phase and 3.04 Å for the Zn-rich phase), which is a consequence of the similarity of atomic size of Pd and Zn (1.40 and 1.35 Å, respectively) as well as electronic effects [31]. Unfortunately this precludes the identification of the correct phase by lattice parameter alone.

From refinements using the neutron data, the fraction of this phase was found to be 4.6 ± 0.7 wt%. The presence of this phase was not obvious in the X-ray diffraction data, nor was it apparent in SEM or BSE images. However, for consistency, the cubic phase was included in the refinements of the X-ray data, where the weight

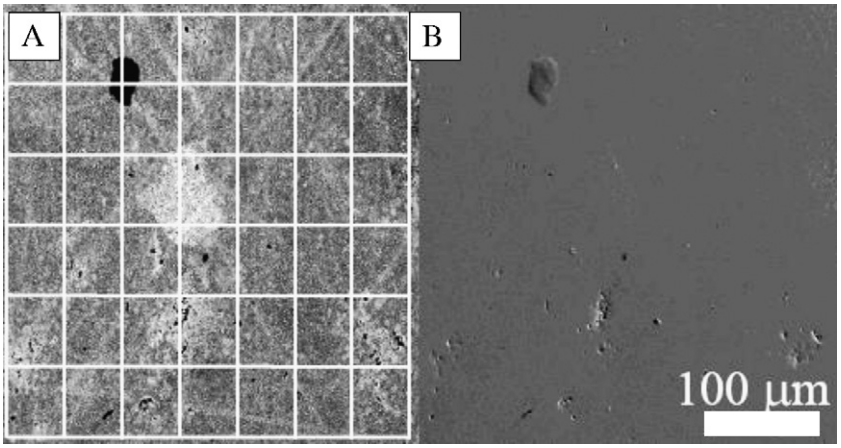

Fig. 4. Backscatter electron (A) and secondary electron (B) images of the polished PdZn surface. Electron microprobe analyses were collected on the grid at 50 μm steps. Light regions are approximately 1% rich in Pd over the mean value of 50.4 at% Pd.

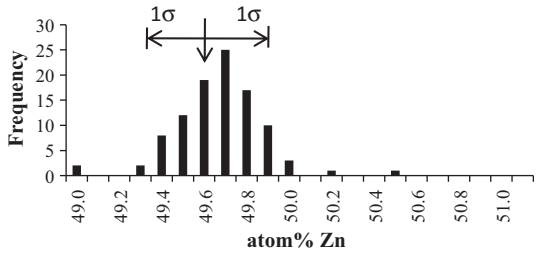

Fig. 5. Mean chemical composition ($\overline{X}$) and chemical variation ($\pm 1\sigma$) of the aerosol powder, reduced at 500 °C for 4 h in 5% H_2/N_2. Analyses were performed on grids at 50 μm intervals.

fraction was refined to be only 1.3 wt%, with the strongest peak from the cubic phase indistinguishable from the background. The possibility of neutrons having a greater sensitivity to the presence of the cubic phase than X-rays was addressed by comparing the ratio of calculated intensities for the cubic (1 1 0) peak and the tetragonal (1 0 1) peak (the most intense peaks for both phases), calculated for neutron and for X-ray diffraction. Structure factor calculations were performed for tetragonal PdZn (50 at% Zn) and both Pd-rich (33.3% Zn (atomic)) and Zn-rich (66.7 at% Zn (atomic)) cubic phases. The sensitivity to detection of the cubic phase can be quantified by the ratio

$$\frac{12 \times F^2_{\text{calc,cubic(1 1 0)}}}{8 \times F^2_{\text{calc,tetragonal(1 0 1)}}} = \frac{I_{\text{calc,cubic(1 1 0)}}}{I_{\text{calc,tetragonal(1 0 1)}}}$$

where 12 and 8 are the reflection multiplicity factors. For neutron scattering, the sensitivity ratios were found to be 1.32 and 1.26 for the Pd-rich and Zn-rich cubic phases, respectively; because of the similar neutron scattering cross-sections for Pd and Zn (Table 1), it is expected that neutron diffraction sensitivity to Pd-rich and Zn-rich phases with the same structure should be similar. In the case of X-ray scattering, the sensitivity ratios were 1.69 for the Pd-rich and 1.03 for the Zn-rich cubic phases, showing that X-ray scattering is more sensitive than neutron scattering to the presence of the Pd-rich cubic phase, but less sensitive than neutron scattering to the presence of the Zn-rich cubic phase. The observation that the cubic phase (1 1 0) peak is readily apparent in the neutron data, but less so in the X-ray data, suggests that the cubic phase in this sample is $PdZn_2$ (β′). An overall thermal parameter was refined for the cubic phase atoms.

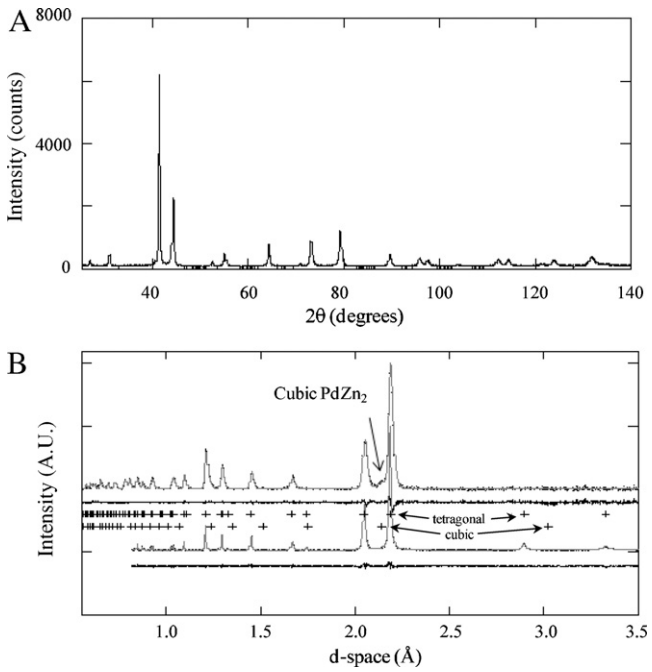

Fig. 6. (A) Experimental X-ray diffraction pattern for β_1 PdZn. (B) Observed, calculated and difference plots for the detector bank-4 neutron data and the X-ray data. The (+) markers show peak positions for the tetragonal (upper) and cubic (lower) phases.

3.2.2. Tetragonal phase (β_1)

The phase of interest for catalysis spans the composition range 37–56 at% Zn [24–27], has the AuCu prototype structure, and is commonly given the designation β_1. This phase carries the Strukturbericht designation $L1_0$ and the Pearson symbol tP2 or tP4, depending upon the unit cell chosen to describe the structure [4,8]. The tP2 structure can be described as a tetragonally distorted CsCl structure with Pd at the cell corners and a Zn atom at the body center. Alternatively, the tP4 structure is comprised of a tetragonally distorted pseudo F.C.C. structure with Pd occupying corner sites and the centers of two opposing faces, and Zn atoms occupy the centers of the four remaining faces. The difference between the tP2 and tP4 structures is that the latter structure allows more crystallographic degrees of freedom, with Pd atoms occupying two crystallographically independent sites. However, in either representation of the structure the atomic positions are fixed by symmetry. (The inverse structure could also be employed, exchanging Pd for Zn, with Zn occupying the two unique sites.) The tP2 structure was employed in our refinements. A feature of β_1 PdZn is its large compositional

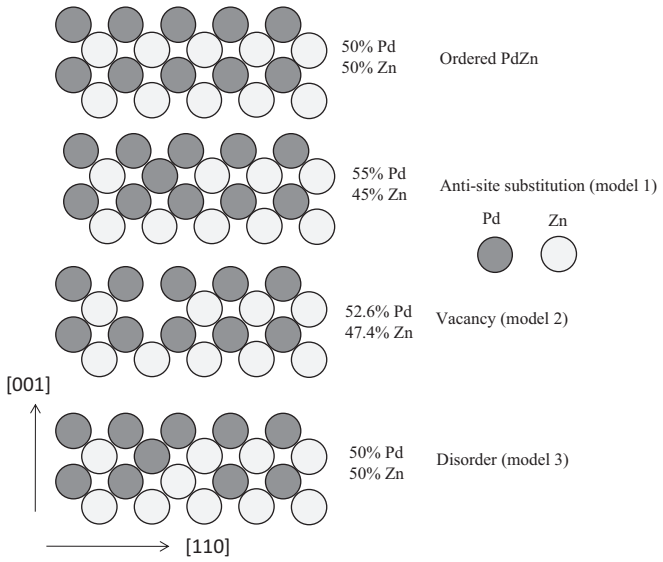

Fig. 7. Possible variations of Pd and Zn atom arrangements in PdZn.

single phase stability range (36–56 at% Zn), suggesting that defects such as vacancies and/or antisite substitution of Pd for Zn and vice versa may be important in this phase. An anti-site substitution model has been proposed for non-stoichiometric β_1 PdZn on the basis of lattice parameter variation with Zn composition [32].

Because of the presence of finely divided, ~5 wt% cubic phase, the EPMA analysis is representative of the bulk composition, rather than the composition of the 1:1 PdZn phase. The EPMA composition can be corrected to represent that of the 1:1 PdZn phase if the composition of the cubic phase is known. In Section 3.2.1 it was shown that the cubic phase composition is probably close to $PdZn_2$, so the bulk EPMA value was corrected accordingly to account for the presence of 5 wt% $PdZn_2$. For refinements using the neutron data, anisotropic thermal parameters for the Pd and Zn sites were used for the tetragonal β_1 phase. Because the neutron diffraction data was collected at 4 K, this should represent a lower bound for the tetragonal β_1 PdZn thermal parameters. For refinements using the X-ray diffraction data, an isotropic overall thermal parameter was initially refined; however, this was found to result in an unrealistically small thermal parameter value, and the isotropic overall thermal parameter was also found to be correlated with the site occupancies. The thermal parameters in the refinement of the X-ray data were therefore fixed at the anisotropic thermal parameter values that had been obtained from refinement of the neutron data. Three site-occupancy models were used in the analysis of the X-ray and neutron diffraction data: (1) varying the Pd:Zn ratio via anti-site substitution of Pd for Zn and vice versa, (2) varying the Pd:Zn ratio via vacancy on either the Pd or the Zn-site, (3) holding the Pd:Zn ratio constant at 1:1 and exchanging Pd on the Pd-site with Zn on the Zn-site. For case (3), a disorder parameter was defined as follows:

$$\text{Disorder} = \frac{Pd_{Zn} + Zn_{Pd}}{Pd_{Pd} + Zn_{Zn}} \quad (1)$$

where Pd_{Pd} is the occupancy of Pd on the Pd-site, Zn_{Zn} is the occupancy of Zn on the Zn-site, Pd_{Zn} is the occupancy of Pd on the Zn-site, and Zn_{Pd} is the occupancy of Zn on the Pd-site. The three models are illustrated schematically in Fig. 7.

Because the X-ray scattering contrast between Pd and Zn is atomic number-dependent, X-ray diffraction Bragg peak intensities are expected to be sensitive to Pd/Zn-site disorder as well as anti-site substitution of Pd for Zn (and vice versa). X-ray peak intensities should also be sensitive to vacancies on the Zn-site (i.e. Zn occupancy <1), but unable to distinguish Pd-site vacancies from anti-site substitution of Zn for Pd. In the case of neutron scattering, however, scattering lengths and cross-sections are quite similar for Pd and Zn (Table 1). As a result, neutron diffraction Bragg peak intensities are relatively insensitive to site disorder or anti-site substitution in PdZn phases, but should be sensitive to vacancies on either the Pd or the Zn site, serving to complement the X-ray data. To test these models, Rietveld refinements were performed for a range of fixed Pd:Zn compositions that were varied according to the three occupancy models described above. The minima in the goodness-of-fit (GOF) parameter (reduced χ^2), plotted as a function of composition, were compared to the known β_1 PdZn composition to evaluate the plausibility of each model.

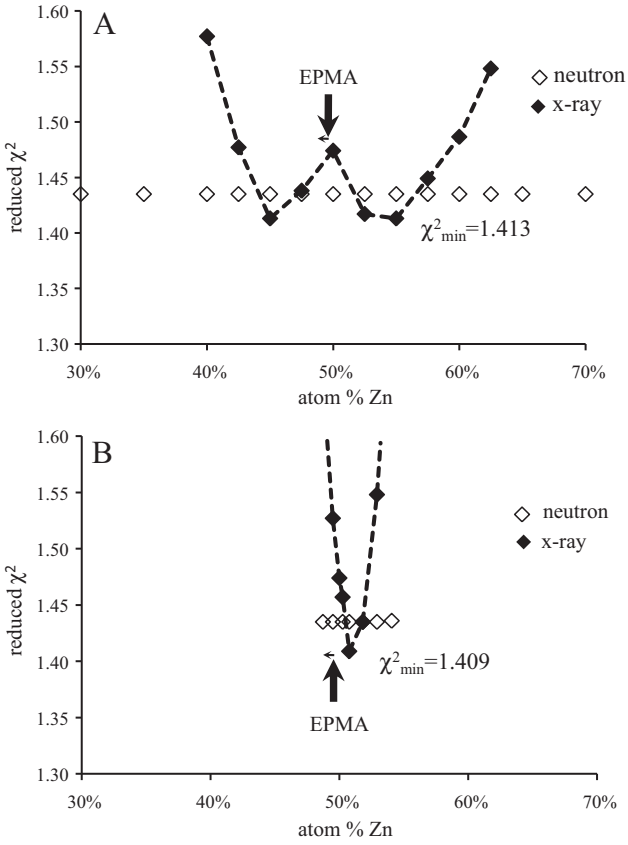

Fig. 8. (A) Variation of the reduced χ^2 parameter with composition for model 1 (anti-site substitution of Pd for Zn and vice versa). (B) Variation of the reduced χ^2 parameter with composition for model 2 (vacancy on either the Pd or the Zn-site). The lateral arrow associated with the EPMA value represents the PdZn composition that would be obtained by the correction of the EPMA value to account for the presence of 5 wt% $PdZn_2$.

Fig. 8A shows the results of refinements using the anti-site Pd–Zn substitution model, compared to the chemical composition as measured by electron microprobe analysis (bulk composition) and as-corrected for the presence of 5 wt% $PdZn_2$ (β_1 PdZn composition). For a perfectly ordered PdZn specimen, one would expect a single GOF minimum, located at 50 at% Zn. In fact, two minima in the GOF data at approximately ±5 at% from the observed composition can be seen for the refinements of the XRD anti-site model data, and the observed composition is located at a local maximum in the GOF parameter, close to a composition of 50 at% Zn. This indicates that a model of perfectly ordered tetragonal PdZn does not adequately explain the data. The GOF for refinements of the neutron diffraction data, using model 1, was found to be independent of composition, as expected from the lack of Pd and Zn neutron scattering contrast. The results of refinements using the vacancy model

Table 3
Refinement statistics.

XRD	Model 1 (antisite)					Model 2 (vacancy)					Model 3 (disorder)
Atom% Zn	45.0				55.0	50.8					50.0
Variables	16				16	16					16
χ^2 min	1.413				1.413	1.409					1.4079
R_{wp} min	0.1064				0.1066	0.1062					0.1062
R_{exp} min	0.0533				0.0534	0.0535					0.0535
Reflections	62				62	62					62
NPD	Model 1 (antisite)					Model 2 (vacancy)					
Atom% Zn	50.0					50.0					
Variables	128					128					
χ^2 min	1.435					1.435					
Banks	1	2	3	4	Σ	1	2	3	4	Σ	
R_{wp} min	0.0251	0.0237	0.0224	0.0249	0.0241	0.0251	0.0237	0.0224	0.0249	0.0241	
R_{exp} min	0.0175	0.0165	0.0156	0.0174	0.0168	0.0175	0.0165	0.0156	0.0174	0.0168	
D_{wd}	1.219	1.466	1.553	1.313	1.375	1.219	1.466	1.553	1.313	1.375	
Reflections	157	157	122	125		157	157	122	125		

are shown in Fig. 8B. For this model, a sharp minimum in the GOF parameter for the X-ray data refinements was found at a composition of 50.8 at% Zn. However, the observed β_1 PdZn composition lies a significant distance from the observed GOF minimum. Also, the GOF parameter for the refinements of the neutron diffraction data was found to be independent of composition for the vacancy model; if vacancies were a significant phenomenon in this sample, one would expect it to be manifested by a minimum in the neutron data GOF.

Fig. 9 shows the variation of the X-ray data refinement GOF parameter with the model 3 disorder parameter (as defined above) for a fixed β_1 PdZn composition of 50 at% Zn, with a minimum located at a disorder parameter value of 0.03. The minimum GOF value of 1.409 is less than or equal to the minimum values that were obtained using models 1 and 2, which means that model 3 accounts for the X-ray diffraction data at least as well as models 1 and 2. Model 3 also satisfies the additional constraint of being close to the observed composition, indicating that model 3 (i.e. a small amount of Pd–Zn disorder) best describes the state of the sample. The statistics for refinement that was performed at the GOF minima for the X-ray data refinements are listed in Table 3, and refined crystallographic data is summarized in Table 4. Because there were no GOF minima in the refinements of the neutron data, neutron

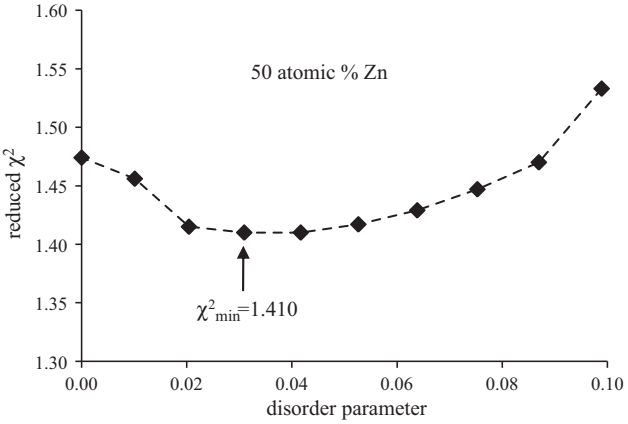

Fig. 9. Variation of the reduced χ^2 parameter with disorder for model 3 (concomitant exchange of Zn for Pd on the Pd-site and Pd for Zn on the Zn-site, for a fixed 50:50 Pd:Zn atomic composition). The disorder parameter is defined as $(Pd_{Zn} + Zn_{Pd})/(Pd_{Pd} + Zn_{Zn})$, where Pd_{Zn} is the fraction of Pd on the nominal Zn-site, Zn_{Pd} is the fraction of Zn on the nominal Pd-site, Pd_{Pd} is the fraction of Pd on the nominal Pd-site, and Zn_{Zn} is the fraction of Zn on the nominal Zn-site.

Table 4
Neutron (NPD) and X-ray (XRD) powder diffraction crystallographic data for bulk PdZn.

Space group	*P*4/*mmm*			
	Lattice parameters			
	NPD (4 K) (Å)	XRD (RT) (Å)		
a	2.89458(3)	2.89917(7)[a]		
c	3.32724(7)	3.3331(2)[a]		
	Atomic positions		Occupancies (model 3)	
Atom site	Wyckoff position	(*x*, *y*, *z*)	Pd	Zn
Pd	1a	(0,0,0)	0.96	0.04
Zn	1d	(1/2, 1/2, 1/2)	0.04	0.96
Thermal parameters	NPD (4 K) (Å^2)	XRD		
Pd U_{11}	0.0052(1)			
Pd U_{22}	0.0052(1)			
Pd U_{33}	0.0046(2)	(Fixed at NPD values)		
Zn U_{11}	0.0049(1)			
Zn U_{22}	0.0049(1)			
Zn U_{33}	0.0062(2)			

[a] SRM640C NIST silicon (a = 5.431195 Å) internal standard.

Table 5
NPD and XRD size parameters and sizes.

	GSAS neutron profile function 4			
	Gaussian size coefficient		Lorentzian size coefficient	
	σ_2^2	Size[a] (Å)	γ_2	Size[b] (Å)
NPD 153° bank	11(1)	575(5)	4.4(2)	1023(50)
NPD −153° bank	14(2)	519(5)	4.5(3)	1000(55)
NPD 90° bank	8(1)	471(3)	4.4(1)	730(19)
NPD −90° bank	8(1)	473(4)	4.5(1)	716(21)

	GSAS X-ray profile function 4 Lorentzian size coefficient	
	L_X	Size[c] (Å)
XRD	22.0(3)	401(5)

$k = 0.9$ (Scherrer's constant); $\lambda = 1.540562$ Å (Cu Kα_1).

[a] $p = (\text{DIFC} \times k)/\sqrt{8(\ln 2)\sigma_2^2}$.

[b] $p = \text{DIFC} \times k/\gamma_2$.

[c] $p = 18,000 \times k \times \lambda/\gamma_2$.

statistics and crystallographic data are listed for refinements at the composition of 50 at% Zn.

The DFT optimized lattice parameters for stochiometric and ordered tetragonal ($P4/mmm$) $Pd_{50}Zn_{50}$ are $a = 2.920$ Å and $c = 3.412$ Å, consistent with previous theoretical work [5] and experiment ($a = 2.899$ Å and $c = 3.295$ Å) [4,22], as well as our experimental values (4 K) ($a = 2.89458(3)$ Å and $c = 3.32724(7)$ Å). This slight overestimation of lattice parameters is typical for calculations at the GGA-level [19]. We also find that the stochiometric and ordered $L1_0$ phase of PdZn is 0.57 eV/atom more stable than the energy of a mechanical mixture of hcp-Zn and fcc-Pd at the same composition. This large stabilization energy indicates the strong affinity of Pd and Zn to form an alloy. In comparison we find that cubic-B2 PdZn is also strongly stabilized, by 0.56 eV/atom, 10 meV less than the tetragonal $L1_0$ phase. Thus, the $L1_0$ structure is expected to be the stable phase at low temperature and the cubic phase may be thermally stabilized at elevated temperatures, consistent with the phase diagram for the Pd–Zn system [24–27]. The calculated energetics for disorder due to Pd ↔ Zn exchange shows that a single exchange is energetically disadvantageous by 1.4 eV/32 atoms for the exchange of nearest neighbors (Pd,Zn)-pairs. This energy depends only weakly on the distance of the exchanged (Pd,Zn)-pairs, it increases by only 0.1 eV/32 atoms as (Pd,Zn)-pairs with the largest possible separation under periodic image convention are exchanged. This high energy associated with disordering leads to the expectation that $Pd_{50}Zn_{50}$ should only possess a small amount of (Pd,Zn) disorder, corroborating the interpretation of our neutron and X-ray diffraction experiments.

3.2.3. Crystallite size

Average tetragonal β_1 PdZn crystallite sizes were extracted from the profile parameters that were refined for the X-ray and neutron diffraction data sets, and are listed in Table 5. Sizes obtained from refinements using the X-ray and neutron data sets are in reasonable agreement with each other. The observed 40–50 nm sizes indicate that the larger particles seen in Fig. 4 are polycrystalline. Comparison of the 40–50 nm crystallite sizes, obtained from the diffraction data, to the average particle size of 126 nm, obtained from the BET measurement also suggest that individual particles are composed of several crystallites. As mentioned above, for consistency the cubic phase was included in the refinements using the X-ray diffraction data as well as the neutron diffraction data, even though its presence in the X-ray data was not readily apparent. Because of the low peak to background ratio for the cubic phase in the X-ray data, the crystallite size profile parameter for the cubic phase was fixed at a value that was consistent with the crystallite size obtained from refinements using the neutron data (9–14 nm).

3.2.4. Microstrain

An anisotropic microstrain model [11] was employed in refinements using both X-ray and neutron data sets. The refined microstrain parameters are listed in Table 6, and the microstrain is

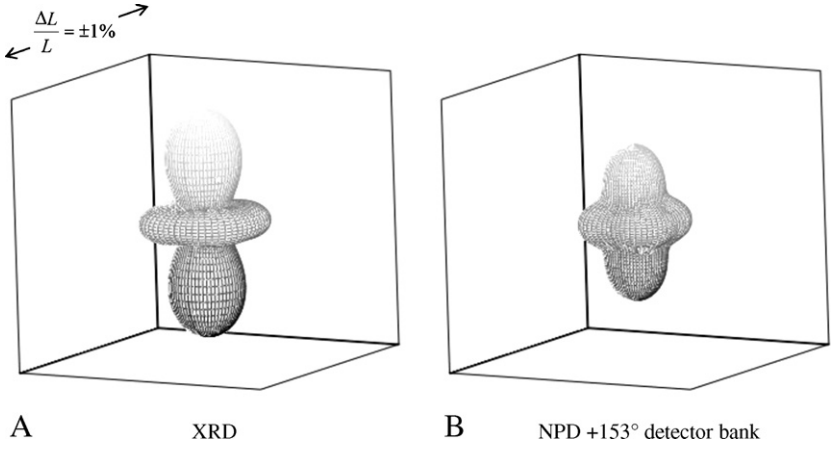

Fig. 10. Graphical representation of the microstrain, obtained from the XRD data (A) and the NPD +153° detector bank (B), which is similar to plots obtained from the NPD −153° and the ±90° detector banks. The edges of the boxes represent ±1% $\Delta l/l$.

Table 6
Neutron diffractometer constants (DIFC) and NPD and XRD anisotropic microstrain parameters.

	DIFC	S400	S004	S220	S202	η
NPD 153° bank	5048	5.1(3)	7.5(4)	6.0(5)	−0.6(2)	1.00(2)
NPD −153° bank	5050	3.8(3)	8.3(5)	6.0(5)	−1.2(2)	1.00(3)
NPD 90° bank	3585	2.0(1)	4.1(2)	2.3(2)	−0.1(1)	1.00(2)
NPD −90° bank	3586	1.5(2)	3.5(1)	1.8(2)	−0.2(2)	1.00(2)
XRD		10.4(6)	21(1)	9.0(6)	−6.7(4)	0.66(2)

shown graphically in Fig. 10. The microstrain obtained from the X-ray data is qualitatively similar to that obtained from the neutron data in that it exhibits a high degree of anisotropy. Quantitative $\Delta l/l$ values along the *c*-axis are ±0.9% (X-ray) and ±0.6% (neutron), which are large. Microstrain has been shown to result from chemical effects [33] and/or mechanical effects [34]. In Ref. [34] it is proposed that nucleation of nanocrystalline α' phase in Ga-stabilized δ plutonium is responsible for microstrain values up to nearly ±0.2% $\Delta l/l$. It is possible that nucleation of nanocrystalline cubic $PdZn_2$ (β') is similarly responsible for the observed large anisotropic microstrain that is seen in β_1 PdZn. Chemical effects would be expected to be less important in β_1 PdZn, due to the size similarity of Pd and Zn.

4. Conclusions

We have demonstrated that powders of PdZn catalyst of controlled composition can be prepared using an aerosol synthesis method. The high surface area coupled with atomic scale mixing allow for relatively rapid (4 h) and low temperature (500 °C) formation of powders composed of 95–99 wt% β_1 PdZn, with minor (1–5 wt%) β'' $PdZn_2$ present as a secondary phase. The rapid formation of β_1 PdZn at relatively low temperature has been shown to result in minimal loss of volatile Zn. Rietveld refinements of neutron and X-ray diffraction data, coupled with electron microprobe analysis, indicate that a small amount of disorder and little or no vacancies are present in β_1 PdZn of composition 50 at% Zn, synthesized under these conditions. The observed small amount of disorder is consistent with the result of our first-principle simulations that predict a high energy penalty for Pd ↔ Zn exchange. We report an experimental X-ray diffraction pattern that is in good agreement with the ICDD calculated reference pattern (PDF number 01-072-2936).

The catalytic performance of this powder is currently being investigated and will be described elsewhere [35].

Acknowledgements

Financial support for this work was provided by the US Department of Energy, Grant DE-FG02-05ER15712. Additional support was provided by the US Department of Energy, EPSCoR Grant DE-FG02-08ER46530. We gratefully acknowledge computing resources provided by the New Mexico Computing Applications Center (NMCAC) on Encanto. A portion of the research was performed using EMSL, a national scientific user facility sponsored by the Department of Energy's Office of Biological and Environmental Research and located at Pacific Northwest National Laboratory.

Appendix A. Supplementary data

Supplementary data associated with this article can be found, in the online version, at doi:10.1016/j.jallcom.2010.09.149.

References

[1] N. Iwasa, T. Akazawa, S. Ohyama, K. Fujikawa, N. Takezawa, Reaction Kinetics and Catalysis Letters 55 (1995) 245–250.
[2] T. Conant, A.M. Karim, V. Lebarbier, Y. Wang, F. Girgsdies, R. Schlogl, A. Datye, Journal of Catalysis 257 (2008) 64–70.
[3] N. Iwasa, S. Masuda, N. Ogawa, N. Takezawa, Applied Catalysis A-General 125 (1995) 145–157.
[4] A.P. Tsai, S. Kameoka, Y. Ishii, Journal of the Physical Society of Japan 73 (2004) 3270–3273.
[5] Z.X. Chen, K.M. Neyman, A.B. Gordienko, N. Rosch, Physical Review B 68 (2003).
[6] A. Karim, T. Conant, A. Datye, Journal of Catalysis 243 (2006) 420–427.
[7] T.T. Kodas, M.J. Hampden-Smith, Aerosol Processing of Materials, Wiley-VCH, New York, 1999.
[8] H. Nowotny, H. Bittner, Monatshefte Fur Chemie 81 (1950) 679–680.
[9] T. Hahn, A.J.C. Wilson, A.A. Authier, M.G. Rossmann, E. Arnold, International Tables for Crystallography, third rev. ed., Kluwer Academic Publishers, Dordrecht/Boston, 1992.
[10] A.C. Larson, R.B. VonDreele, General Structure Analysis System (GSAS), Los Alamos National Laboratory, 2004, Report LAUR 86-748.
[11] P.W. Stephens, Journal of Applied Crystallography 32 (1999) 281–289.
[12] V.F. Sears, Neutron News 3 (1992) 29–37.
[13] P. Hohenberg, W. Kohn, Physical Review B 136 (1964).
[14] G. Kresse, J. Furthmuller, Computational Materials Science 6 (1996) 15–50.
[15] G. Kresse, J. Hafner, Physical Review B 48 (1993) 13115–13118.
[16] G. Kresse, J. Hafner, Journal of Physics-Condensed Matter 6 (1994) 8245–8257.
[17] J.P. Perdew, K. Burke, M. Ernzerhof, Physical Review Letters 77 (1996) 3865–3868.
[18] P.E. Blochl, Physical Review B 50 (1994) 17953–17979.
[19] G. Kresse, D. Joubert, Physical Review B 59 (1999) 1758–1775.
[20] M. Methfessel, A.T. Paxton, Physical Review B 40 (1989) 3616–3621.
[21] H.J. Monkhorst, J.D. Pack, Physical Review B 13 (1976) 5188–5192.
[22] W.B. Pearson, Handbook of Lattice Spacings and Structures of Metals, first ed., Pergamon Press, New York, 1967.
[23] G. Ertl, H. Knözinger, J. Weitkamp, Handbook of heterogeneous catalysis, VCH, Weinheim, 1997.
[24] e.-i.-c.P. Villars, in: s.e. Okamoto, K. Cenzual (Eds.), PdZn Phase Diagram, ASM International, 2006.
[25] T.B. Massalski, Binary Alloy Phase Diagrams, second ed., Materials Information Society, Materials Park, OH, 1990.
[26] M. Hansen, Constitution of Binary Alloys, second ed., McGraw-Hill, New York/Toronto/London, 1958.
[27] H. Okamoto, Pd–Zn (Palladium–Zinc), second ed., ASM International, 1990.
[28] H. Nowotny, E. Bauer, A. Stempfl, Monatshefte Fur Chemie 82 (1951) 1086–1093.
[29] H.H. Stadelmaier, W.K. Hardy, Zeitschrift Fur Metallkunde 52 (1961) 391–396.
[30] K.M. Alasafi, T. Chattopadhyay, K. Schubert, Journal of the Less-Common Metals 59 (1978) P41–P50.
[31] J.P. Neumann, H. Ipser, Y.A. Chang, Journal of the Less-Common Metals 57 (1978) P29–P37.
[32] S. Kou, Y.A. Chang, Acta Metallurgica 23 (1975) 1185–1190.
[33] E.J. Peterson, W.L. Hults, M. Simpson, J.Y. Coulter, J.L. Smith, Advances in X-ray Analysis 45 (2002) 238–244.
[34] A.C. Lawson, J.A. Roberts, B. Martinez, R.B. Von Dreele, B. Storey, H.T. Hawkins, M. Ramos, F.G. Hampel, C.C. Davis, R.A. Pereyra, J.N. Mitchell, F. Freibert, S.M. Valone, T.N. Claytor, D.A. Viskoe, F.W. Schonfeld, Philosophical Magazine 85 (2005) 2007–2022.
[35] B. Halevi, E.J. Peterson, A. DeLariva, E.W. Jeroro, V. Lebarbier, Y.Y. Wang, J.M. Vohs, B. Kiefer, E. Kunkes, M. Havecker, M. Behrens, R. Schlögl, A.K. Datye, Journal of Chemical Physics C 114 (2010) 17181–17190.